

Characterization and Prediction of Flow Behavior in High-Manganese Twinning Induced Plasticity Steels: Part I. Mechanism Maps and Work-Hardening Behavior

A. SAEED-AKBARI, L. MOSECKER, A. SCHWEDT, and W. BLECK

Thermodynamic stacking fault energy (SFE) maps were developed using the subregular solution model for the Fe-Mn-Al-C system. These maps were used to explain the variations in the work-hardening behavior of high-manganese steels, both through experiments and by comparison with the published data. The suppression of the transformation induced plasticity (TRIP) mechanism, the similarity between the shape of the work-hardening rate diagrams for the produced iso-SFE materials, and an earlier onset of stage C of work hardening by decreasing SFE were shown to be efficiently predictable by the given mechanism maps. To overcome the limitations arising from studying the deformation response of high-manganese steels by SFE values alone, for example, the different work-hardening rate of iso-SFE materials, an empirical criterion for the occurrence of short-range ordering (SRO) and the consequently enhanced work-hardening, was proposed. The calculated values based on this criterion were superimposed on the thermodynamics-based mechanism maps to establish a more accurate basis for material design in high-manganese iron-based systems. Finally, the given methodology is able to clarify the work-hardening behavior of high-manganese twinning induced plasticity (TWIP) steels across an extensive range of chemical compositions.

DOI: 10.1007/s11661-011-0993-4

© The Minerals, Metals & Materials Society and ASM International 2011

I. INTRODUCTION

THE recently developed twinning induced plasticity (TWIP) steels are a class of high-manganese (> 15 wt pct manganese) austenitic steels with superior mechanical properties such as ultrahigh strength and high formability. These steels have potential applications in the auto industry, due to their increased strength-to-weight ratio and excellent energy absorption properties.^[1-4] In these materials, a proper combination of alloying elements (such as manganese, aluminum, and carbon) increases the thermal or mechanical stability of the face-centered-cubic (fcc) austenite γ phase, to the extent that no athermal or deformation-induced hexagonal-close-packed (hcp) martensitic transformation can occur. The possible range of chemical compositions in which the hcp (ϵ) martensite formation is suppressed can be efficiently predicted using the appropriate thermodynamic models and parameters and the resultant mechanism maps.^[5-7] The mechanism maps developed through the thermodynamics-based approach^[5] not only show the existence range of transformation induced

plasticity (TRIP) mechanisms, but also demonstrate the variations in the stacking fault energy (SFE) by changing the chemical composition and temperature. Therefore, they were proposed as the practical tools for the tailored materials design in low-SFE austenitic systems.

The main requirement for the activation of supportive deformation mechanisms for dislocation gliding, such as deformation-induced twinning and martensite formation, is a low SFE value. Both TWIP and TRIP mechanisms (mechanical twinning and ϵ martensite formation) are related to the dissociation of perfect dislocations into Shockley partials with a Burgers vector of type $\mathbf{b} = \frac{1}{6}\langle 112 \rangle$ and, thus, are related to the energy of the created stacking faults (SFs).^[8] The crystallographic changes associated with the formation of a twin or ϵ martensite plate are explained in terms of the arrangement of SFs: identical Shockley partial dislocations are packed on every close-packed $\{111\}$ plane for a twin and on every second close-packed $\{111\}$ plane for ϵ martensite.^[9,10] Therefore, the active plasticity mode is directly related to the SF probability and the SFE value.^[3,11-13] In the proposed model by Mahajan and Chin, a three-layer fault formed by the dislocation reaction $\frac{1}{2}\langle 01\bar{1} \rangle + \frac{1}{2}\langle 10\bar{1} \rangle \rightarrow 3 \times \frac{1}{6}\langle 11\bar{2} \rangle$ can act as an embryonic twin.^[14] Based on this model, the embryonic three-layer faults that are distributed throughout the slipped region grow into each other, leading to the formation of macroscopic twins. This approach was successfully employed by Kibey *et al.*^[15] to establish a model for the prediction of twinning stress in fcc metals. Nevertheless, the specific dislocation interactions that

A. SAEED-AKBARI, Postdoctoral Researcher and Research Team Leader, L. MOSECKER, Doctoral Candidate and Project Engineer, and W. BLECK, University Professor and Department Head, are with the Department of Ferrous Metallurgy, RWTH Aachen University, 52072 Aachen, Germany. Contact e-mail: alireza.saeed-akbari@iehk.rwth-aachen.de A. SCHWEDT, Head of the Scanning Electron Microscopy Group, is with the Central Facility for Electron Microscopy (GFE), RWTH Aachen University, 552074 Aachen, Germany.

Manuscript submitted August 16, 2010.

Article published online December 23, 2011

result in the formation of twins in high-manganese TWIP steels were not clear until the recent publication of three works by Idrissi *et al.*^[10,16,17] In this extensive trilogy, the possible mechanisms of deformation twinning in fcc metals were reviewed, and the twins' internal structure was correlated with the work-hardening rate of TWIP steels. They described major differences in the observed twins in the Fe-Mn-C and Fe-Mn-Si-Al systems and related them to the variation of the work-hardening behavior of these steels. By comparing Fe-Mn-C and Fe-Mn-Si-Al TWIP steels, Idrissi *et al.*^[16] also showed that the twins formed in the Fe-Mn-C system are thinner and contain a much larger density of sessile defects; thus, they are much stronger than in the Fe-Mn-Si-Al steel. Moreover, the critical stress required for the plastic deformation of the twin lamellae was lower in Fe-Mn-Si-Al steel than in Fe-Mn-C steel, which led to a considerable difference between the work-hardening behavior of the two materials. It was also suggested that carbon-manganese interactions could influence the dislocation reactions required for the occurrence of faulted twins.

It had been reported that with decreasing SFE, the deformation mechanisms are activated in the following order: dislocation glide \rightarrow dislocation glide + mechanical twinning \rightarrow dislocation glide + martensitic transformation.^[3,18,19] In addition, an increase in the operating temperature leads to an increase of the SFE value. Within the range of SFEs close to the upper limit of the TRIP mechanism (~ 20 mJ/m²),^[5] deformation twinning becomes operational. This activation results in the simultaneous presence of TRIP and TWIP mechanisms in a narrow range of SFE values.^[18,20] Also, other important microstructural parameters such as grain size^[21,22] and local stress and strain significantly impact the deformation mechanism.^[23] The dynamic Hall-Petch effect,^[3,4,24] a result of deformation twinning, causes rapid accumulation and storage of dislocations in which the twin boundaries act as strong barriers against dislocation motion, similar to grain boundaries.^[25] Consequently, deformation twinning in highly alloyed low-SFE steels enhances the work hardening of samples during tensile testing. Adler *et al.*^[26] suggested that the upward trend of flow curves in tensile testing is affected by the combination of the softening effect of deformation twinning—as a supportive deformation mechanism—and the hardening effect of the twinned microstructure, as discussed earlier.

Nevertheless, according to Stepanskiy,^[27] the factors that control the level and dynamics of work hardening in austenitic steels are as follows: (a) the SFE value, (b) the ε martensite start temperature, and (c) the initiation temperature of the serrated plastic flow. The serrated flow suggests another proposed mechanism of work hardening in TWIP steels besides deformation twinning. In high-manganese Fe-Mn-C and Fe-Mn-Al-C steels, the interaction of short-range ordering (SRO) or clustering of alloying elements^[28] with extended (such as in the low-SFE TWIP steels)^[25] or complete dislocations (such as in the high-SFE microband induced plasticity (MBIP) steels) is expected to produce a SFE-independent^[29] planar glide mechanism that enhances the work hardening.^[29–31] In their pioneering work, Dastur and Leslie^[32] argued that deformation twinning is not the

primary factor in the rapid work hardening of Hadfield steels. Their hypothesis, which was supported by Zuidema *et al.*,^[33] Gerold and Karnthaler,^[28] Shun *et al.*,^[34] Chen *et al.*,^[25] and recently Kim *et al.*,^[35] explains the high affinity of carbon and manganese atoms to generate clusters. In these clusters, carbon occupies the octahedral interstitial sites, and manganese atoms occupy the six nearest neighbor sites with an occupancy higher than the expected value based on the atomic concentration of manganese. The interaction between ordered zones with extended dislocations and continuous disordering by the passage of leading and trailing partial dislocations generates conditions in which the required stress for the glide of subsequent dislocations gradually decreases, leading to planar glide. The increased planar glide described in this theory results in a higher level of work hardening. Finally, Chen *et al.*^[25] discussed the interaction between the carbon-manganese octahedral clusters and the mobile extended dislocations. Not only is this interaction the primary reason for the planar dislocation glide, but it also explains other phenomena, such as dynamic strain aging (DSA) and the resultant jerky flow behavior in high-manganese TWIP steels.

In the present work, the effects of chemical composition and applied parameters such as temperature, strain rate, and grain size on the work-hardening behavior of TWIP steels are experimentally reviewed from the viewpoint of the previously developed mechanism maps,^[5] which are further updated to account for different work-hardening mechanisms such as deformation twinning and planar glide. These maps are shown to be able to predict thermodynamically and empirically the deformation response of TWIP steels. Finally, the role of the studied parameters on changing the shape of the work-hardening rate diagrams are schematically presented in conjunction with the published data concerning different stages of the work hardening in TWIP steels.

II. EXPERIMENTAL PROCEDURE

A. Materials and Tensile Tests

Six grades of high-manganese austenitic TWIP steels (E1 through E6) with the nominal chemical compositions given in Table I were used. The as-received materials consisted of hot-rolled (2- to 2.4-mm thickness, HR) and cold-rolled (1.2-mm thickness, CR) sheets in the Fe-Mn-C and Fe-Mn-Al-C systems. The cold-rolled grades were annealed (AN) at 1073 K (800 °C) for 30 minutes to achieve a fully recrystallized microstructure. In addition, some selected high-manganese austenitic steels described in the literature (L1 through L4 in Table II) were used to check the consistency of the developed design and characterization methodology for the TWIP steels used in this work with those used in other investigations.

The tensile testing specimens were machined along the rolling direction according to two different standards, as given in Figure 1. The variations in the applied tensile sample geometry (A30 and A50) and the as-received state (HR and CR) were used to test the applicability of

Table I. Nominal Chemical Composition of TWIP Steels Used in the Current Work*

Material	Composition (Weight Percent)					Condition	SFE (mJ/m ²)	TOI (—)
	Mn	Al	C	Fe				
E1	22	—	0.6	bal		2.4 mm–HR	27	0.12
E2	28	—	0.3	bal		2.4 mm–HR	27	0.05
E3-1 E3-2	19	—	0.6	bal		1.2 mm–CR/AN 2.4 mm–HR	21	0.14
E4-1 E4-2	24	—	0.7	bal		1.2 mm–CR/AN 2.4 mm–HR	35	0.13
E5	24	—	0.6	bal		2.0 mm–HR	31	0.11
E6	27	3.5	0.4	bal		2.0 mm–HR	50	0.07

*E_i, HR, CR, and AN stand for the experimental material number *i* and hot-rolled, cold-rolled, and annealed conditions, respectively. E5 and E6 grades were also used in Part II of the present work for further discussions. The SFE (at 300 K (27 °C)) and TOI values are discussed in Section III.

Table II. Nominal Chemical Compositions of Selected Literature-Reported TWIP Steels for Comparison*

Material	Composition (Weight Percent)					Condition	SFE (mJ/m ²)	TOI (—)
	Mn	Al	C	Fe				
L1 ^[25,36]	18	—	0.6	bal		X–CR/AN	19	0.15
L2 ^[35,36]	18	1.5	0.6	bal		X–CR/AN	29	0.15
L3 ^[37]	20	—	1.2	bal		1.2 mm–CR/AN	44	0.27
L4 ^[38]	12	—	1.2	bal		1.4 mm–CR/AN	35	0.46

*“X” stands for the unknown thickness of the sheets in the referenced work. The SFE (at 300 K (27 °C)) and TOI values are discussed in Section III.

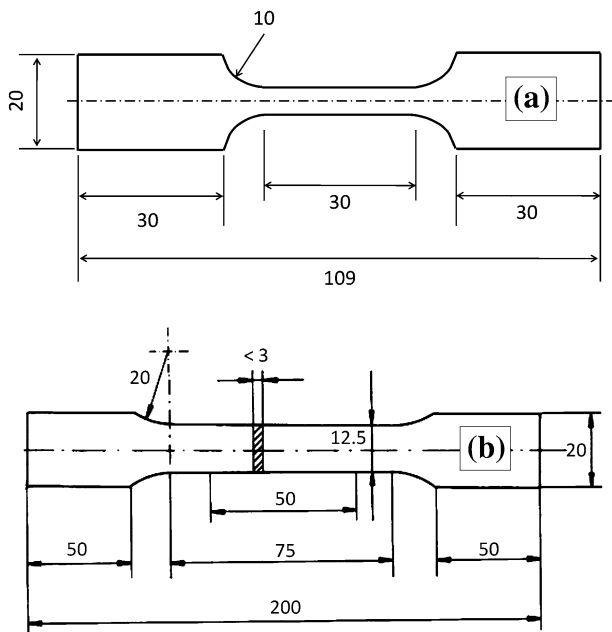


Fig. 1—(a) A30 tensile sample used for the experiments on compositions E1, E2, E3-1, and E4-1 and (b) A50 tensile sample used for investigation on E3-2, E4-2, E5, and E6 steels. All units are millimeters.

our predictions over a broad range of parameters. Nevertheless, the direct comparison between the work-hardening behavior of the experimental materials was made only between samples with the same as-received conditions and tensile geometry.

The tensile tests at temperatures of 233 K (–40 °C), 300 K (27 °C), and 373 K (100 °C) were carried out using a Zwick Z100/TL3S universal tensile testing machine (Zwick GmbH & Co. KG, Ulm, Germany). Adjusted crosshead displacement rates of 1.8 to 5.4 mm/min for the A30 samples and 0.3 to 30 mm/min for the A50 samples were used to achieve applied strain rates of (SR, $\dot{\epsilon}$) of 0.001 to 0.003 s^{–1} for the E1 through E4 steels and 0.0001 to 0.01 s^{–1} for the E5 and E6 steels. During the experiments, the length and the width changes of the tensile specimens were recorded using a high-resolution video extensometer (Messphysic Materials Testing GmbH, Fürstenfeld, Austria). The stress and strain values were then measured using Xpert software (Zwick GmbH & Co. KG, Ulm, Germany).

B. Microstructural Analysis

Microstructural investigations were carried out on the HR samples using electron backscatter diffraction (EBSD). To prepare the specimens, the mounted samples were mechanically polished with diamond pastes of 6 and 1 μ m after grinding. The specimens were further electropolished with electrolyte A2 from Struers (Struers GmbH, Willich, Germany). The electropolishing was performed between 3 and 6 K by applying a voltage potential of 34 V for 15 seconds. The EBSD measurements were performed by a JEOL*

*JEOL is a trademark of Japan Electron Optics Ltd., Tokyo.

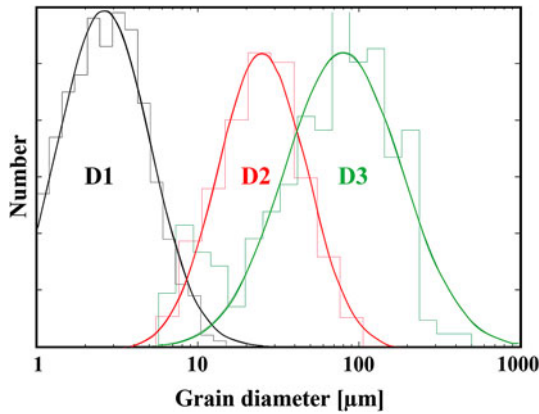


Fig. 2—Three grain-size distributions of the E5 samples used in the current work.

JSM 7000F FEG-SEM with an EDAX-TSL DigiView III detector and OIM DataCollection 5.2/OIM Analysis 5.2 software. Measurements were made at a voltage of 25 kV with a probe current of approximately 10 nA. The area and step size of each measurement were individually adjusted, with step size ranging from 25 to 200 nm depending on the grain size and degree of deformation. EBSD analysis was performed by considering all scanned points with a confidence index (CI) between 0.1 and 1.0. The criterion for the definition of twin boundaries was 60 deg misorientation about the $\langle 111 \rangle$ axis, with an angular tolerance of 5 deg within the austenitic (fcc) matrix. The as-received E5 samples had three types of grain-size distributions (as given in Figure 2), which were called D1, D2, and D3. Using the Jeffries planimetric procedure per the ASTM E 112-96 (2004) standard,^[39] the average austenite grain size of the experimental HR steels was calculated to be approximately 35 to 40 μm and approximately 15 μm for CR/AN samples.

In Section III, a theoretical basis for the prediction of work-hardening behavior in TWIP steels (across the range of chemical compositions and temperatures) is established, which is followed by the experimental verification in Section IV.

III. MECHANISM MAPS AND PREDICTION OF WORK-HARDENING BEHAVIOR

The systematic development of composition- and temperature-dependent SFE maps was initially discussed by Saeed-Akbari *et al.*^[5] to show the possibility of steel design based on thermodynamic calculations. It was shown that the composition- and temperature-dependent upper limits of the TRIP mechanism could be empirically modeled by considering the variations in the iso-SFE domains within the mentioned maps. The calculated results of the mentioned model were in good agreement with the available experimental results in the literature.

A. SFE Calculation for the Fe-Mn-Al-C System

In the present work, the mechanism maps were developed by switching the thermodynamics-based calculations of the chemical Gibbs free energy to the scientific group Thermodata Europe (SGTE) database^[40] to avoid the overestimations concerning the upper limit of the TRIP mechanism by using the mechanism maps in Reference 5. The core assumption for the mentioned thermodynamics-based calculations is the use of the SFE (Γ) as the required Gibbs free energy to form a platelet of ε martensite with the thickness of two atomic layers within the dense planes.^[3] The proposed equation according to Adler *et al.*^[26] is as follows:

$$\Gamma = 2\rho\Delta G_{\text{eff}}^{\gamma \rightarrow \varepsilon} + 2\sigma^{\gamma/\varepsilon} \quad [1]$$

where ρ is the molar surface density along the $\{111\}$ planes and $\sigma^{\gamma/\varepsilon}$ is the γ/ε interfacial energy. In this model, $\Delta G_{\text{eff}}^{\gamma \rightarrow \varepsilon} = \Delta G_{\text{chem}}^{\gamma \rightarrow \varepsilon} + \Delta G_{\text{mag}}^{\gamma \rightarrow \varepsilon}$, where $\Delta G_{\text{eff}}^{\gamma \rightarrow \varepsilon}$, $\Delta G_{\text{chem}}^{\gamma \rightarrow \varepsilon}$, and $\Delta G_{\text{mag}}^{\gamma \rightarrow \varepsilon}$ are the effective, chemical, and magnetic Gibbs free energy changes during the $\gamma \rightarrow \varepsilon$ transformation, respectively. The required parameters for the calculation of Γ in Eq. [1] were computed using the subregular solution model for the Fe-Mn-Al-C system and the methodology explained by Saeed-Akbari *et al.*^[5,20] The input parameters for the magnetic contributions and the binary interactions of the elements from Reference 41 were used, except for the interfacial energy, $\sigma^{\gamma/\varepsilon}$, which was assumed to be constant and equal to 10 mJ/m^2 . Figure 3 shows the strong dependence of the thermodynamically calculated SFE values on the chemical composition of the high-manganese TWIP steel. With a constant carbon content of 0.6 wt pct (Figure 3(a)), the effect of aluminum addition on the SFE is a monotonic increase that is almost independent of the manganese content. In addition, the increase of the SFE with rising manganese content accelerates markedly for manganese content of more than 17 wt pct. The three-dimensional (3-D) plot in Figure 3(b) defines the iso-SFE surfaces at 0 mJ/m^2 (the lower limit of the thermodynamics-based SFE calculation with a constant interfacial energy, $\sigma^{\gamma/\varepsilon}$, of 10 mJ/m^2) and 20 mJ/m^2 (the upper limit of the TRIP mechanism). The plot illustrates a quaternary (Fe-Mn-Al-C) composition domain with a SFE of 20 to 75 mJ/m^2 in which the TWIP steels can be located.^[42,43] By increasing the aluminum content, it is possible to design TWIP steels with lower manganese or carbon contents as long as the relevant chemical composition is located above the iso-SFE surface of 20 mJ/m^2 . However, as explained previously, the deformation twinning and the strong dependence of this mechanism on the SFE value cannot adequately explain the complicated work-hardening behavior of high-manganese steels across the range of chemical compositions, which is highlighted in Section III-B.^[32,44]

B. Unified Maps for SFE Values and Manganese-Carbon Ordering

In a study of high-manganese Hadfield steel, Karaman *et al.*^[45] summarized that the high work hardening

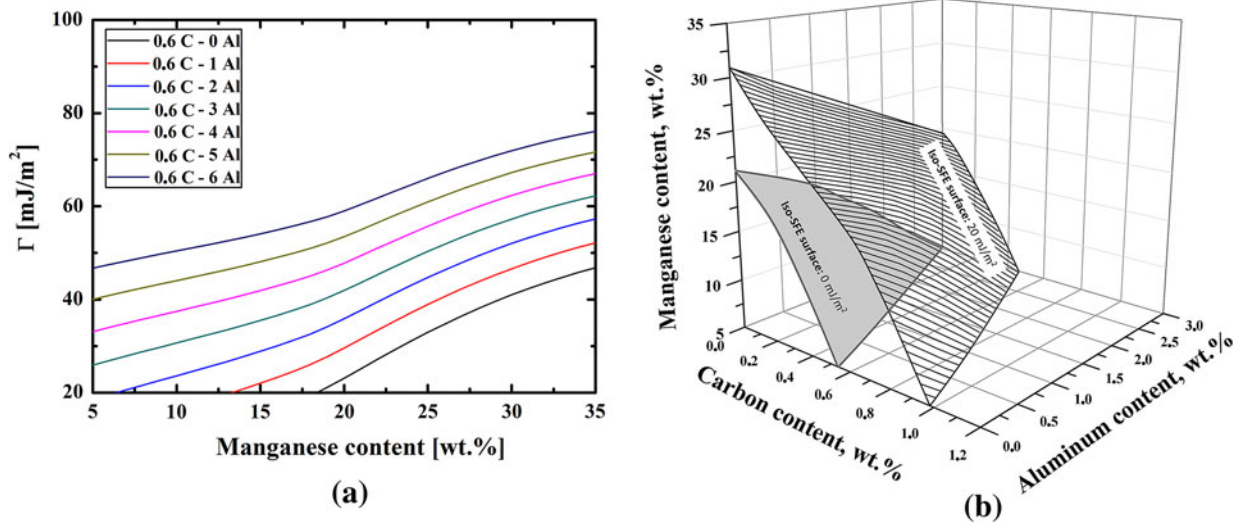


Fig. 3—Effects of chemical composition on the SFE (Γ) value of Fe-Mn-Al-C TWIP steels: (a) with a constant carbon content of 0.6 wt pct and increasing aluminum from 0 to 6 wt pct and (b) by simultaneous change of carbon, manganese, and aluminum content. A SFE of 20 mJ/m² is regarded as the approximate upper limit of ϵ for the TRIP mechanism.^[5]

in such a low SFE material is due to the following: (a) deformation twinning and formation of twinned-untwinned zones inside the grains and the consequent interference of deformation with the twinned zone, (b) dynamic strain aging and the relevant interactions between dislocations and a high concentration of interstitials, (c) exchange of position of carbon atoms from octahedral to tetrahedral sites, and (d) SF formation and the Suzuki^[46] effect. In addition, it has been suggested that to overcome the barrier for SF formation and deformation twinning, the following factors may facilitate the process: the mobility of partial dislocations under applied stress; stress concentration caused by piled-up dislocations at dislocation locks; motion of carbon atoms from octahedral to tetrahedral sites by movement of the leading partial, trapping carbon in a transient structure; and, finally, short-range order caused by manganese-carbon clustering.^[45,47] Furthermore, the effects of carbon and manganese on the deformation response and work-hardening behavior of high-manganese steels have been extensively debated in the literature. In principle, carbon in Fe-Mn-Al-C TWIP steels is thought to define the morphology and the internal structure of twins,^[16] increase the SFE value,^[5,48] and make SRO or SRC zones with manganese, causing the occurrence of the DSA phenomenon and planar dislocation glide.^[25,49] All these mechanisms were found to be beneficial for strengthening or increasing the work hardening of high-manganese steels.

We attempted to combine the strong dependence of high-manganese steel work hardening on the number of manganese-carbon bonds, as reported by Owen and Grujicic,^[50] with the theories that support the prominent effect of deformation twinning, as described by Bouaziz *et al.*^[44] Both approaches were attempted recently by different investigators in attempts to model the flow behavior of TWIP steels. Kim *et al.*^[51] added a DSA-dependent term to the constitutive model of Kubin and

Estrin,^[52,53] and Bouaziz *et al.*^[54] followed a semiempirical methodology to overcome the deficiencies of physical models of flow curves in dealing with different chemical compositions. In the current article, the approach recently proposed by von Appen and Dronskowski^[55] was followed. The most stable SRO zones were assumed to be the octahedral compounds containing one carbon atom surrounded by six next neighbor manganese atoms in the fcc austenite lattice. Based on their *ab initio* calculations, the large energy difference between the CMn₆ and CFe₆ octahedra (in CMn_i, where *i* stands for the number of manganese atoms as next nearest neighbors of a carbon atom) is due to the high driving force for SRO in the former case. This driving force was shown to decrease continuously as the number of manganese atoms in the next nearest neighboring sites of carbon atoms was reduced and independent of carbon or manganese content. In the current work, a semiempirical dimensionless parameter called the “theoretical ordering index” (TOI) was defined according to Eq. [2], which provided a measurement of the fraction of carbon and manganese atoms in different Fe-Mn-C steels:

$$\text{TOI} = \frac{X_C}{X_{\text{Mn}}} = \frac{\sum x_i}{\sum x_i} = \frac{x_C}{x_{\text{Mn}}} = \frac{\frac{N_C}{N}}{\frac{N_{\text{Mn}}}{N}} = \frac{N_C}{N_{\text{Mn}}} \quad [2]$$

where X_i , x_i , and N_i are the molar fraction, number of moles, and number of atoms for element *i*, respectively; N is the Avogadro constant, which is equal to 6.022×10^{23} . The defined TOI—in terms of its dependence on carbon and manganese content—very much resembles the suggested dimensionless parameter called the “equivalent manganese content” by Bouaziz *et al.*^[54] The applied derivation technique and the application of TOI to the explanation of the work-hardening behavior of TWIP steels in the current work are exclusive and

capable of clarifying the possible ambiguities in Reference 54 for the development of a composition-dependent model of flow behavior.

The calculated TOI values were superimposed on the thermodynamics-based mechanism maps for high-manganese steels, and the locations of the chemical compositions from Tables I and II were marked in the maps of Figure 4. For TOI values less than 0.1, more than 10 manganese atoms are available for every carbon atom. Therefore, there is a high probability for the existence of $\text{CFe}_{6-x}\text{Mn}_x$; however, the population of manganese-containing octahedral clusters with 1 carbon and 6 manganese atoms (CMn_6) is very low due to the relative shortage of carbon for the number of manganese atoms in this composition range.

For TOI values between 0.1 and 0.3, the number of manganese atoms per carbon atom varies from 10 to 3. The increase in the number of carbon atoms in this TOI range increases the population of CMn_6 octahedra. In addition, it is crucial to consider the *ab initio* calculations in Reference 55, which indicate that the reaction energies ΔE_R for $\text{CFe}_{6-x}\text{Mn}_x$ clusters with $x \geq 3$ are either negative or close to zero, while ΔE_R is positive for

$x < 3$. Finally, the high concentration of carbon and relative manganese depletion in the TOI range greater than 0.3 lead to a balance of substitutional (manganese) and interstitial (carbon) alloying elements that provides between 1 and 3 manganese atoms for every carbon atom. In this domain, the population of CMn_6 octahedral clusters is likely to decrease; in contrast to the decrease in the TOI range less than 0.1, this decrease is due to the reduction of the number of manganese atoms.

IV. WORK-HARDENING BEHAVIOR OF HIGH-MANGANESE TWIP STEELS

A. Results

1. Effect of TOI (thermodynamically iso-SFE steels E1 and E2)

As seen in Figure 5, the iso-SFE ($\sim 27 \text{ mJ/m}^2$) TWIP steels E1 and E2 showed similar variations of the work-hardening rate during deformation, despite the constantly higher value of approximately 800 MPa for E1 ($\epsilon > 0.10$). In addition, the image quality (IQ) maps

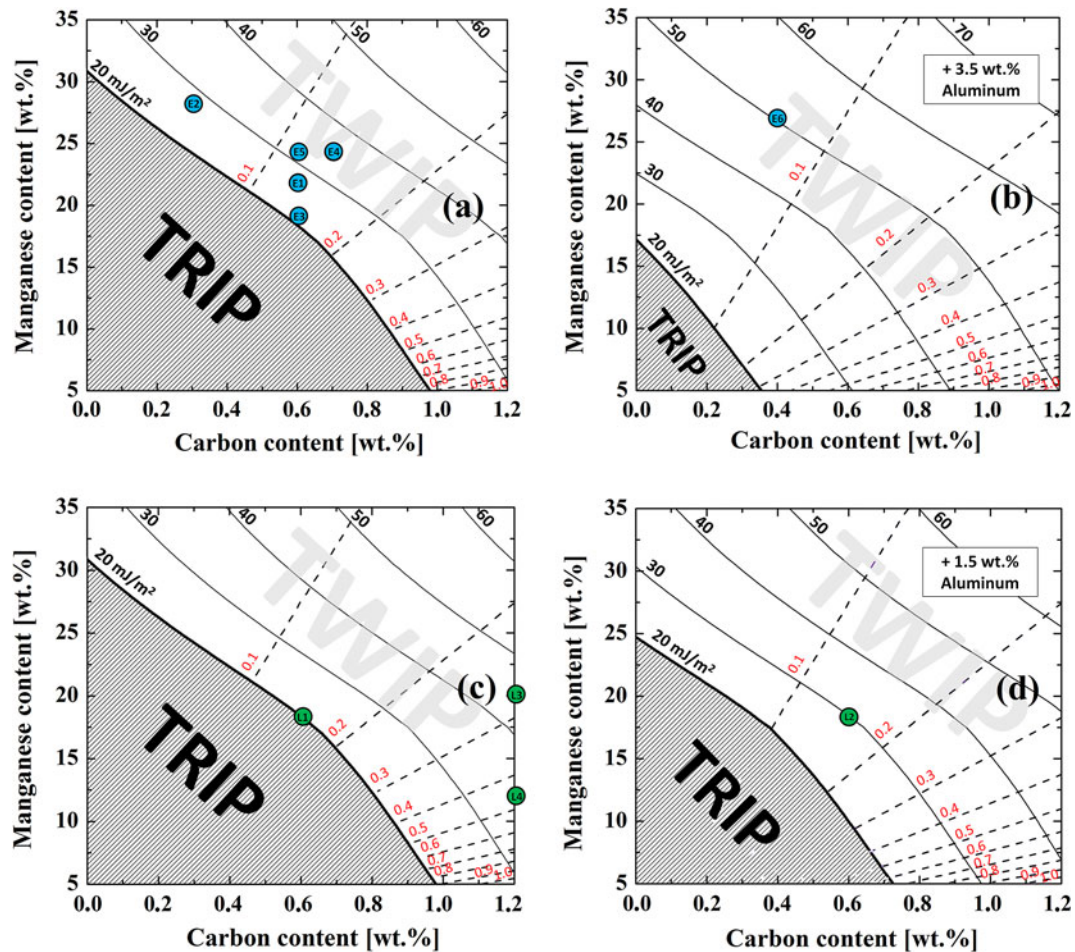


Fig. 4—Thermodynamics-based mechanism maps with the included TOI domains: (a) the Fe-Mn-C system with the location of the experimental steels in the current work, E1 through E5; (b) the Fe-Mn-Al-C system with the experimental steel E6; (c) the Fe-Mn-C system with the high-manganese steels from literature, L1,^[25,36] L3,^[37] and L4,^[38] and (d) the Fe-Mn-Al-C system with the location of the L2 steel from literature.^[35,36] The black and red numbers inside the maps give the SFE and TOI values, respectively.

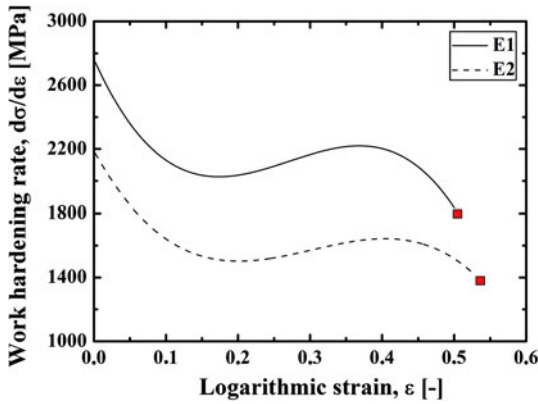


Fig. 5—Work-hardening rate diagrams of HR steels E1 and E2, at 300 K. The red squares indicate the location of the samples taken for the EBSD analysis shown in Fig. 6.

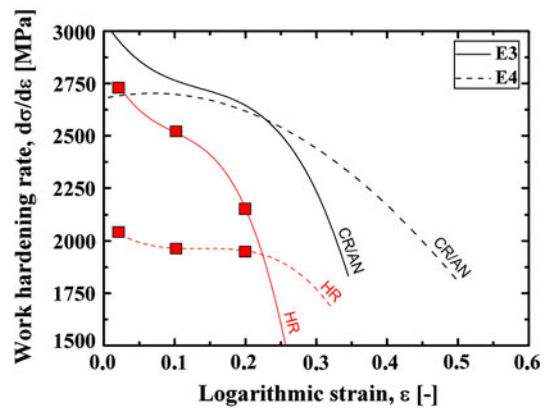


Fig. 7—Work-hardening rate diagrams of CR/AN (black) and HR (red) steels of grades E3 and E4 at 300 K (27 °C). The red squares indicate the location of the samples taken for the EBSD analysis shown in Figs. 8 and 9.

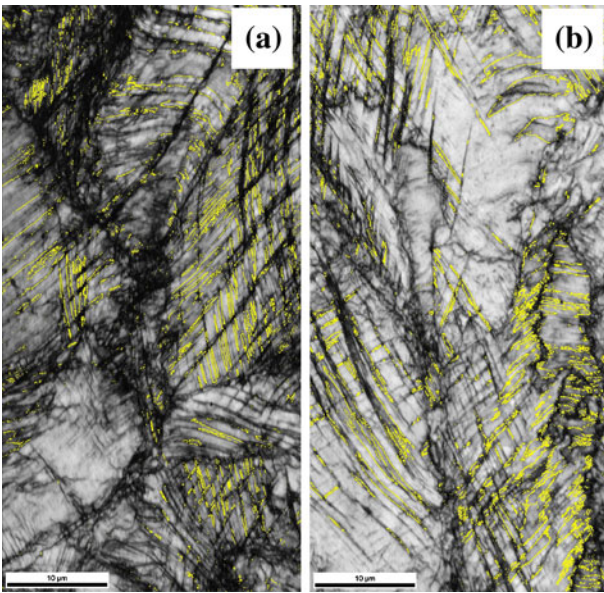


Fig. 6—IQ maps of HR steels (a) E1 and (b) E2 after fracture (red squares in Fig. 5) at 300 K (27 °C). The detectable twin boundaries are marked in yellow based on the criterion given in Section II-B. The scanned area has dimensions of $30 \mu\text{m} \times 60 \mu\text{m}$, step size of 50 nm.

(Figures 6(a) and (b)) of these materials showed the presence of twin boundaries within the austenitic matrix in both cases. An increase in the twin boundaries fraction in the E2 steel compared to the E1 steel was observed based on the applied settings for the EBSD measurement. Nevertheless, it is noteworthy that the E1 steel (Figure 6(a)), which had a higher TOI of 0.12 compared with E2 (TOI = 0.05), showed larger areas of nonindexed zones with $\text{CI} < 0.1$ (black) during the EBSD analysis, which can be related to the strong lattice distortions in these areas.^[56–58]

2. Effect of SFE (iso-TOI steels E3 and E4)

According to Figure 4(a), the E3 and E4 steels had similar TOI values of 0.14 and 0.13, respectively.

However, the SFE value of the E3 steel ($\sim 21 \text{ mJ/m}^2$) is 14 mJ/m^2 lower than that of the E4 steel (35 mJ/m^2). In addition, the work-hardening rate diagrams of these steels, as depicted in Figure 7 for both the HR and CR/AN materials, show a constantly higher level for the E3 steel within the logarithmic strain range below 0.25 and an earlier drop of the work-hardening rate at higher strain values. The E4 steel showed fracture strain values (ϵ_f) that were 0.10 to 0.15 higher than those of the E3 steel for the HR and CR/AN samples. The IQ maps of the E3 (Figure 8) and E4 (Figure 9) steels for logarithmic strains of 0.02, 0.10, and 0.20 presented similar steps in the evolution of deformation twinning, from the onset of twin formation to twin saturation. No indication of higher twinning density for the low SFE E3 steel was found, based on the EBSD results of Figures 8 and 9. However, the limitations of the EBSD technique for the detection of fine deformation twins must be considered. These limitations can result in an erroneously lower estimate for the twinning density in the case of the E3 steel. Recently, the use of low accelerating voltage (5 to 7.5 kV, which is approximately 5 times lower than the values used in the current work) during the EBSD analysis was proposed to improve the spatial resolution and, thereby, detect deformation twins of nanoscopic size.^[59] In any case, such methods are still under development and beyond the scope of the present work.

B. Effects of Manganese and Aluminum (Steels L1 Through L4, E5 and E6)

As depicted in Figures 10(a) (steels L1 and L2) and (b) (steels L3 and L4), the increase of aluminum (with constant manganese and carbon contents) and manganese content (with no aluminum and a constant carbon content) can change the value of the work-hardening rate. Both aluminum and manganese ($< 15 \text{ wt pct}$) are known to increase the SFE value in TWIP steels,^[5–7] but the addition of aluminum to L2 steel decreased the work-hardening rate (as expected for the increase of SFE), while the addition of manganese to L3 steel increased the work-hardening rate. The fracture strain

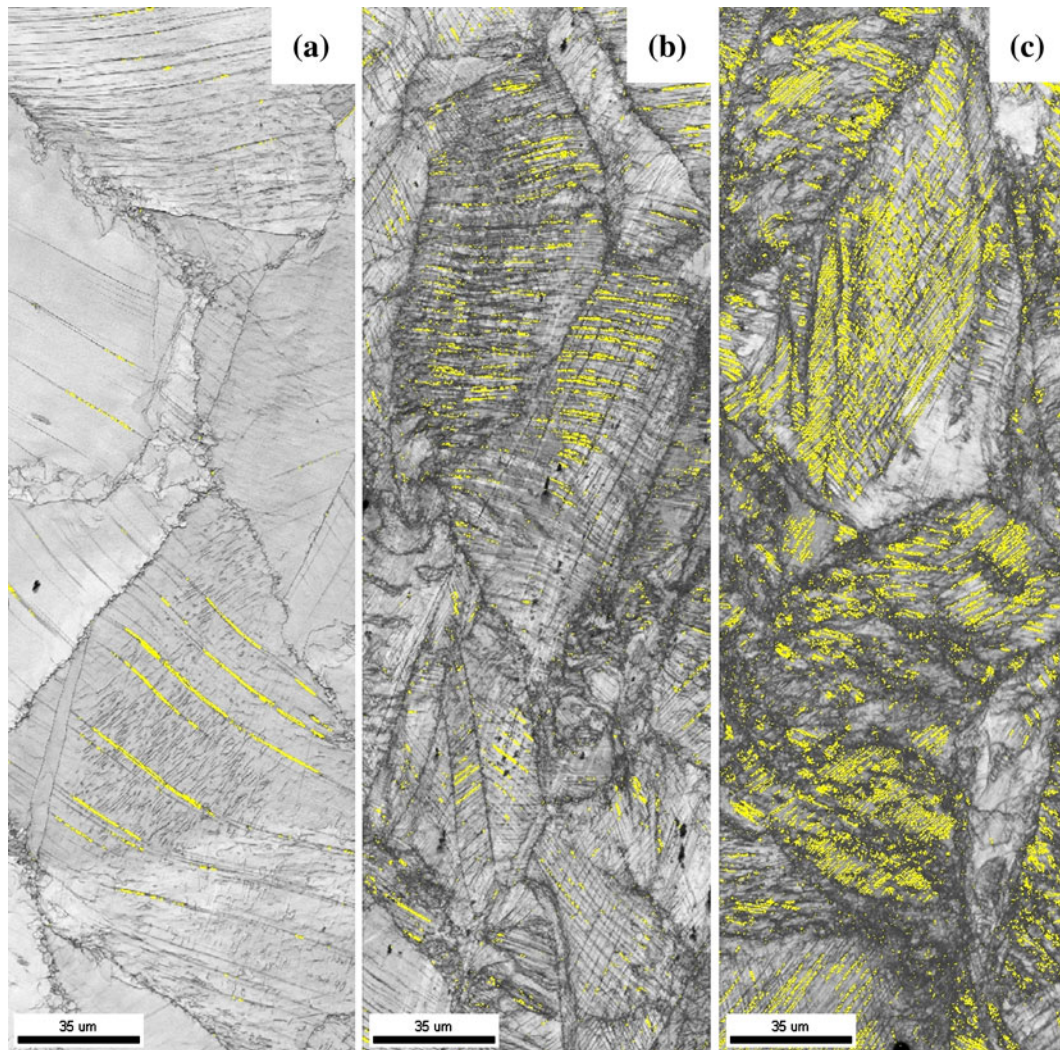


Fig. 8—IQ maps of HR steel E3 after the application of logarithmic strains of (a) $\varepsilon = 0.02$, (b) $\varepsilon = 0.10$, and (c) $\varepsilon = 0.20$ (red squares in Fig. 7) at 300 K (27 °C). The detectable twin boundaries are marked in yellow, based on the criterion given in Section II-B. The scanned area has dimensions of $100 \mu\text{m} \times 300 \mu\text{m}$, step size of 200 nm.

was also improved in the case of L3 steel, resulting in a $\Delta\varepsilon_f$ value of approximately 0.10. In addition, the simultaneous decrease of SFE and increase of TOI in E5 steel relative to E6 steel (Figure 11(a)) resulted in an increase of the logarithmic fracture strain and true fracture stress to $\Delta\varepsilon_f = 0.20$ and $\Delta\sigma_f = 500 \text{ MPa}$, respectively. In addition, aluminum-containing E6 steel showed a nonserrated (smooth) plastic flow (Figure 11(a)), with a lower work-hardening rate of approximately 950 MPa for logarithmic strains of more than 0.10 (Figure 11(b)).

C. Effects of Temperature, Grain Size, and Applied Strain Rate (Steel E5)

The EBSD analysis on the fractured samples of the E5 steel after tensile deformation at 233 K (−40 °C), 300 K (27 °C), and 373 K (100 °C) was performed in three ways: (1) by increasing the deformation temperature (and, consequently, the SFE) from 233 K (−40 °C) to 373 K (100 °C) in the intermediate grain-size regime; (2) by consideration of the increase in the value of the

grain-size distribution from D1 to D3; and (3) by increasing the applied strain rate for a constant temperature and grain-size distribution. The temperature variation within the aforementioned range raised the SFE value from 29 mJ/m^2 at 233 K (−40 °C) to 38 mJ/m^2 at 373 K (100 °C), as seen in the SFE map of Figure 12. According to the given map in Figure 12, the change of the SFE was minor (29 to 31 mJ/m^2) when the temperature was increased from 233 K (−40 °C) to 300 K (27 °C) and became more pronounced (31 to 38 mJ/m^2) as the temperature was further increased to 373 K (100 °C). The work-hardening rate after the initial drop was highest at 233 K (−40 °C) and lowest at 373 K (100 °C), but the tests at 233 K (−40 °C) and 300 K (27 °C) in Figure 13(a) returned almost similar values. The logarithmic fracture strain was found to be inversely proportional to the deformation temperature (and SFE).

The change in the grain-size distribution from D1 to D3 imposed similar variations in the work-hardening rate (Figure 13(b)) as those imposed by a temperature

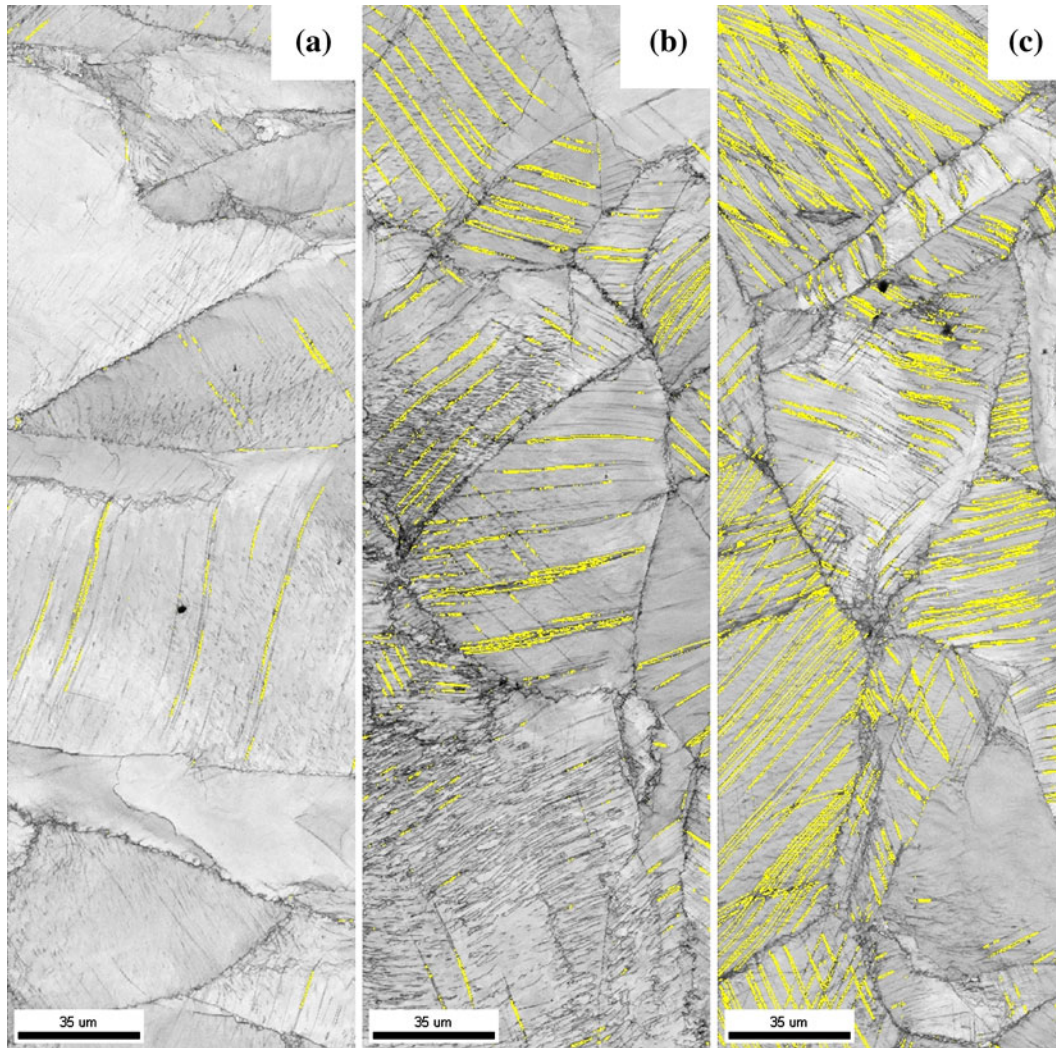


Fig. 9—IQ maps of HR steel E4 after the application of logarithmic strains of (a) $\epsilon = 0.02$, (b) $\epsilon = 0.10$, and (c) $\epsilon = 0.20$ (red-colored squares in Fig. 7) at 300 K (27 °C). The detectable twin boundaries are marked in yellow based on the criterion given in Section II-B. The scanned area has dimensions of $100 \mu\text{m} \times 300 \mu\text{m}$, step size of 200 nm.

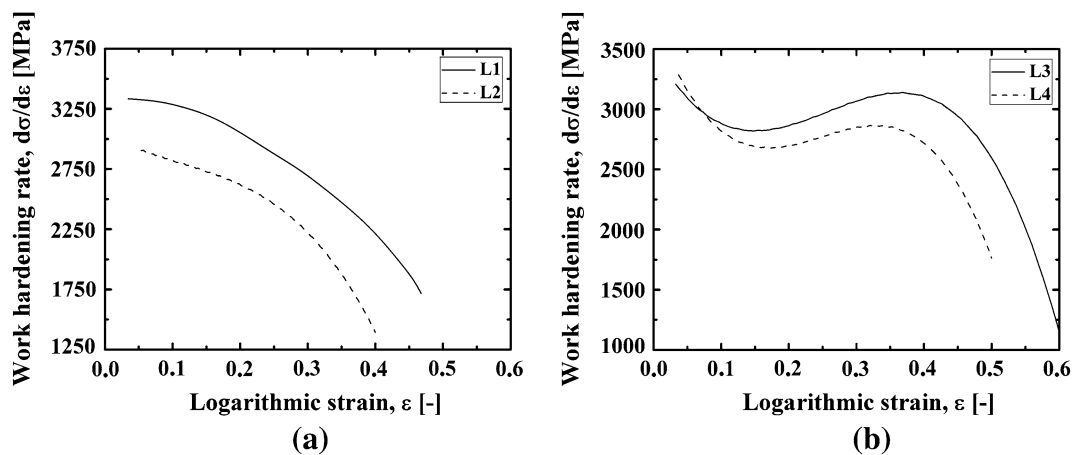


Fig. 10—Work-hardening rate diagrams for steels (a) L1 and L2 and (b) L3 and L4 from the literature.^[25,35–38]

increase (Figure 13(a)). However, the intermediate grain-size regime seemed to enhance slightly the logarithmic fracture strain. The applied strain rate, $\dot{\epsilon}$, in the

range of 0.0001 s^{-1} to 0.001 s^{-1} , did not change the work-hardening rate in a meaningful manner that was consistent with the reportedly low strain-rate sensitivity

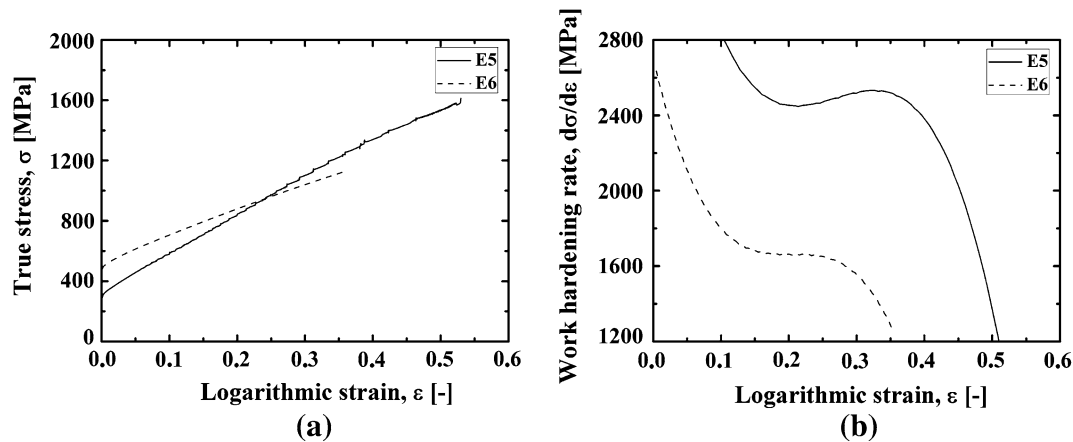


Fig. 11—(a) Flow curves and (b) work-hardening rate diagrams for HR steels E5 (Fe-Mn-C) and E6 (Fe-Mn-Al-C) after the quasi-static tensile tests at 300 K (27 °C).

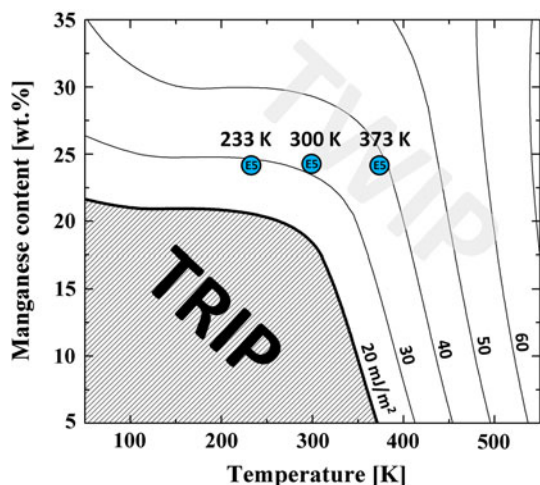


Fig. 12—Thermodynamics-based mechanism map (composition-temperature) with a constant carbon content of 0.6 wt pct: the positions of the E5 steel at increasing temperatures are marked.

of high-manganese steels (Figure 13(c)).^[25,35] Nevertheless, a further increase of the applied strain rate to 0.01 s^{-1} resulted in a decrease of the work-hardening rate, similar to the effect of temperature increase (Figure 13(a)).

In the EBSD IQ maps of Figures 14(a) and 15(a) for the logarithmic strain of 0.02, annealing twin boundaries were observed within the austenitic matrix, while deformation twins were not detected. The lack of deformation twins at the mentioned deformation level could be due to the selected area for the EBSD analysis and not necessarily the lack of activity for this mechanism. In addition, the twins might also be too thin to be detected by EBSD analysis. Deformation twins were recently observed for a logarithmic strain of 0.02 by Barbier *et al.*^[60] and Hamada *et al.*^[61] in TWIP steels, which suggests an early activation of deformation twinning for this group of low-SFE materials. At higher strain levels ($\epsilon = 0.10$), the samples with a coarser grain size (D3, Figure 15(b)) showed the activation of two non-coplanar twin systems (red and white arrows), while in the

case of the finer grain-size regime (D2, Figure 14(b)), the deformation twins were in their early stage of activation (white arrow). In general, a large fraction of the microstructure in D1 (Figure 16) was occupied by detected points with $CI < 0.1$, which are colored black and cannot be used for further discussion. This finding might be due to the large degree of deformation in the fractured ($\epsilon > 0.35$), fine-grained (D1) structure, for which the fine EBSD analysis step size of 25 nm was not sufficiently small to allow exact analysis. Nevertheless, the length of the twin boundaries increased as the grain-size distribution increased from D1 (Figure 16) to D3 (Figure 17). Additionally, the volume fraction of twins and the number of twins per grain, a measure also used by Barnett,^[62] increased in the same direction. This fact can be seen more easily when comparing the EBSD results for the D1 sample (Figure 16(b)) at 373 K (100 °C) with those obtained for the D3 sample (Figure 17(b)) at 373 K (100 °C). The increase of the SFE value (29 to 38 mJ/m^2) as the temperature increased from 233 K (−40 °C) to 373 K (100 °C) did not seem to affect the microstructural twin density in a meaningful way, as seen by comparing Figure 16(a) with 16(b) or Figure 17(a) with 17(b).

However, it must be noted that for a true comparison of the twinning density in the fractured samples ($\epsilon > 0.35$), consideration of the undetected microstructural twins *via* EBSD analysis is crucial but was not investigated in the present work.

V. DISCUSSION

A. Work-hardening Behavior of Iso-SFE TWIP Steels E1 and E2

Based on the definition of the TOI value given in Section III, the E1 and E2 steels have 8 and 20 manganese atoms available, respectively, for every compositional carbon atom. Considering a composition-independent high driving force for the formation of CMn_6 octahedral clusters, as described by von Appen and Dronskowski,^[55] it is assumed that all carbon atoms

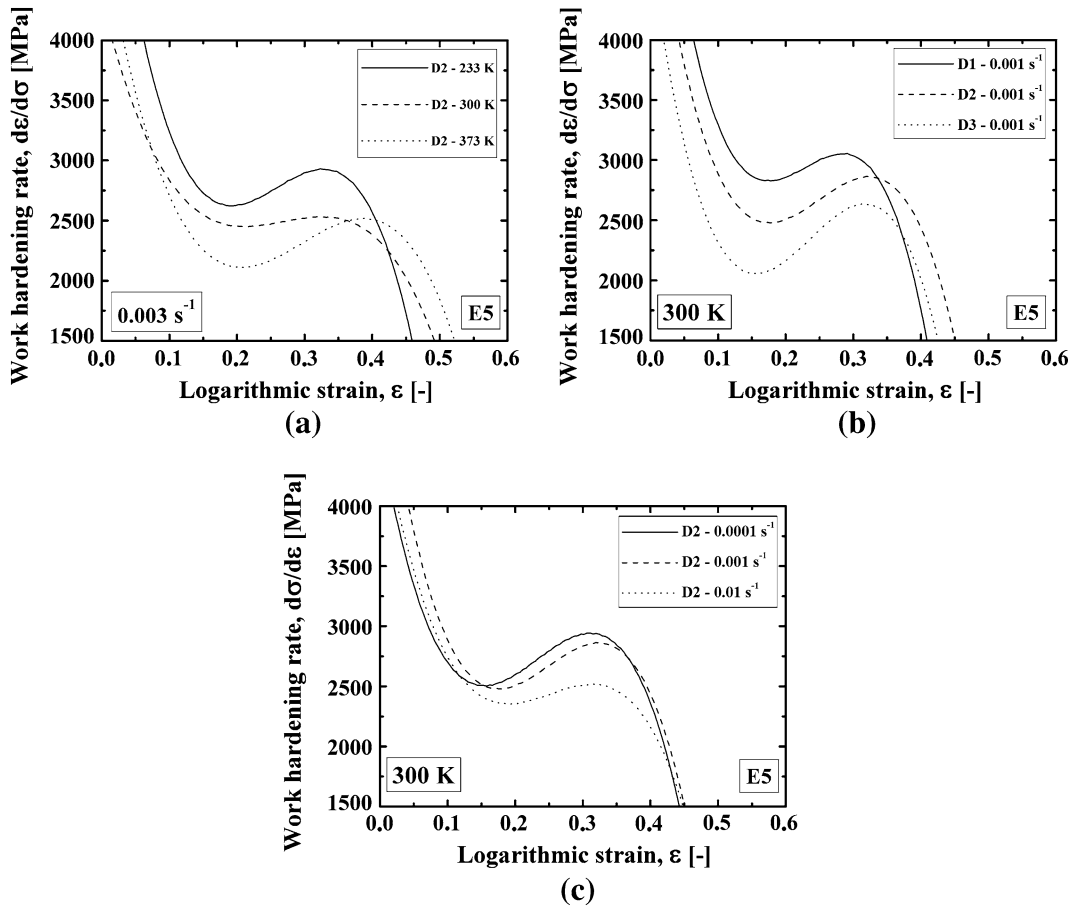


Fig. 13—Work-hardening rate diagrams of HR steel E5 by (a) temperature variation, (b) grain-size variation, and (c) applied strain-rate variation.

(in both E1 and E2) are involved in forming $\text{CFe}_{6-x}\text{Mn}_x$ clusters with some possible configurations seen in Figure 18. Therefore, as a simplifying assumption, we focus on CMn_6 clusters and assume that the variations in the population of other $\text{CFe}_{6-x}\text{Mn}_x$ clusters, if they exist, monotonically follow the population of CMn_6 clusters.

The population of CMn_6 clusters is substantially lower in E2 steel than in E1 steel due to the shortage of carbon atoms in the former case ($\text{TOI} < 0.1$). In addition, it can be proposed that the interstitial occupancy probability ($P_{nC}(n)$ in Eq. [3]) defined by Owen and Grujicic^[50] is reduced in E2 steel compared with E1 for $0 \leq n \leq 6$ because of the decrease in the number of octahedral clusters that contain a carbon atom:

$$P_{nC}(n) = \frac{N_{nC}}{N_n} \quad [3]$$

where N_{nC} is the number of CMn_n octahedral clusters (clusters containing one carbon atom and n manganese atoms) and N_n is the total number of octahedral clusters with n manganese atoms. According to Dastur and Leslie,^[32] the resultant locking of dislocations *via* the reorientation of carbon-manganese couples in the core of mobile dislocations results in an increase in the dislocation density for a given strain, thereby increasing

the work hardening of high-manganese steels. This phenomenon can be interpreted as the cause for the higher work-hardening rate in E1 steel compared with E2 steel and the presumably stronger lattice distortion in the IQ maps of Figure 6(a). Furthermore, other observations concerning the role of solute atoms and the SRO regions on SFE values and deformation twinning must not be neglected. Based on the explanations of Petrov,^[63] the thermodynamically calculated SFE values based on a regular, solid solution^[5,7,41,64] deviate from reality. Specifically, for higher interstitial content (>1.50 at. pct), deviations occur because of the changes in the electronic structure of the solid solution^[63] caused by increasing the interstitial solute content. This factor means that E2 steel with an interstitial solute (carbon) concentration of 1.38 at. pct can be adequately described by the assumption of regularity, while E1 steel with a carbon concentration of approximately 2.70 at. pct deviates from the regular solution model and the resultant SFE value. The segregation of solutes to the SFs (Suzuki effect)^[46,65] reportedly decreases the SFE value^[66] for the dilute solutions,^[67] while in the more concentrated solid solutions, if any appreciable local order exists, the so-called Fisher interaction^[68] between the SRO regions and the extended dislocations significantly contributes to the strengthening.^[69] The Suzuki effect can have a measurable strengthening role

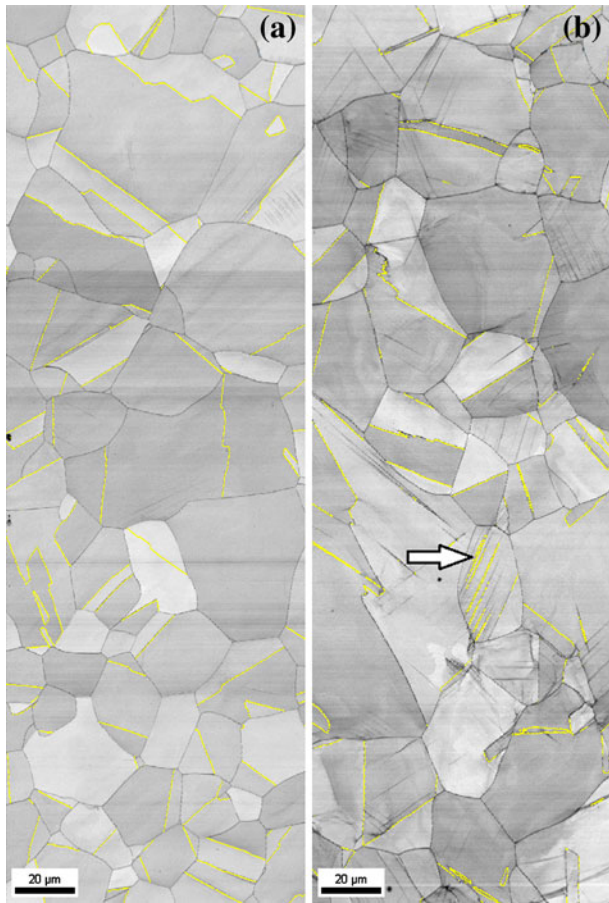


Fig. 14—IQ maps of HR steel E5 deformed at 300 K (27 °C) by an SR ($\dot{\epsilon}$) of 0.003 s^{-1} for the D2 grain-size distribution: (a) $\epsilon = 0.02$ and (b) $\epsilon = 0.10$. The detectable twin boundaries are marked in yellow. The scanned area has dimensions of $100 \mu\text{m} \times 300 \mu\text{m}$, step size of 200 nm.

only when a sufficiently high density of dislocations causes the SFs to nearly overlap.^[70] The two mechanisms—Suzuki and Fisher—can also be regarded as somewhat interconnected, as the nucleation of SRO can occur preferentially on the SFs because of the Suzuki interaction.^[71] Despite the effect of the Suzuki mechanism, causing a clear decrease of the SFE value, the influence of SRO on the SFE and deformation twinning has been the subject of debate. While an earlier work by Thomas^[72] suggests the increase of SFE by SRO, a later extensive report by Pepplewell and Crane^[73] defines SRO as an extremely potent hardening mechanism, acting by decreasing the local SFE value and the local lattice distortion resulting from the strain field of the ordered regions. Moreover, it was proven that the size or the number of ordered regions specifies the amount of the resultant strengthening by SRO.^[73] In the present work, the E1 steel, which is expected to have a higher population of $\text{CFe}_{6-x}\text{Mn}_x$ ordered zones than the E2 steel (because of a higher TOI value), showed a higher fraction of points with $\text{CI} < 0.10$, which could be related to a higher lattice distortion imposed by the strain field of the SRO regions. The lower observed fraction of deformation twins in the E1 steel than in the E2 steel

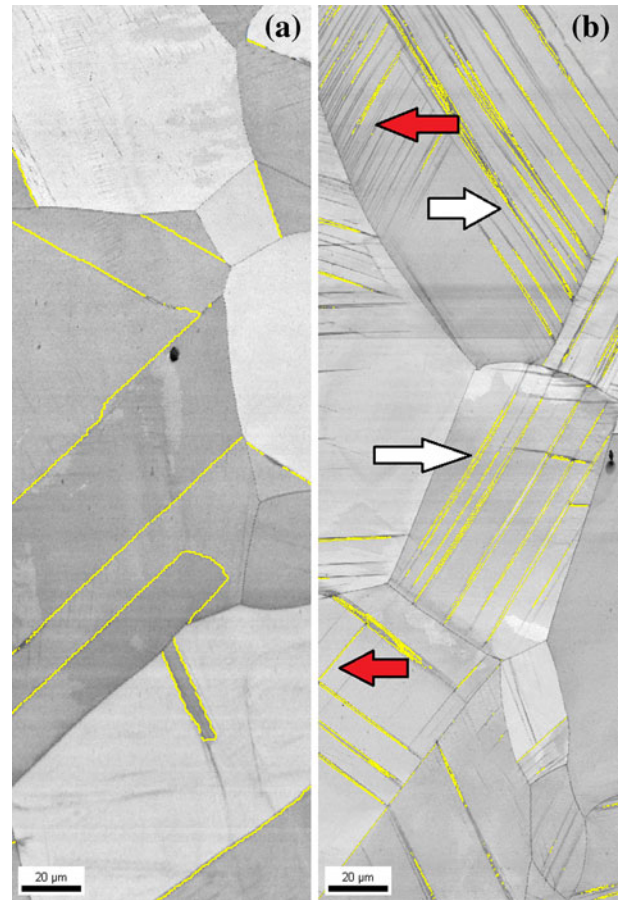


Fig. 15—IQ maps of HR steel E5 deformed at 300 K (27 °C) by an SR ($\dot{\epsilon}$) of 0.003 s^{-1} for the D3 grain-size distribution: (a) $\epsilon = 0.02$ and (b) $\epsilon = 0.10$. The detectable twin boundaries are marked in yellow. The scanned area has dimensions of $300 \mu\text{m} \times 700 \mu\text{m}$, step size of 500 nm.

(ignoring the detection limitations of EBSD) can be explained by the effect of SRO on the twinning stress. Karaman *et al.*^[74] argued that in the intermediate SFE regime for nitrogen-containing stainless steel single crystals, the SRO of nitrogen and chromium results in increased twinning stress because of the requirement that SRO be destroyed in the successive twin planes during twin growth.^[74] On the other hand, a further decrease of SFE, by increasing the nitrogen content, results in more pronounced deformation twinning as the dislocation glide becomes almost as difficult as twin nucleation.^[74] This phenomenon was shown to be the result of the competitive nature of different mechanisms, such as strain aging, planar glide, and deformation twinning, in the range of SFE values and solute concentrations. Therefore, as E1 steel—based on the subregular solution model of Eq. [1]—had an SFE value of 27 mJ/m^2 and a much higher population of SRO regions, it had a slightly lower twinning density compared with the E2 steel due to an increase in twinning stress in the former case. This analysis can be correct only if the Suzuki effect on the SFE for the more dilute alloy (E2) balances the SRO effect on the SFE for the more concentrated alloy (E1) so that the main governing

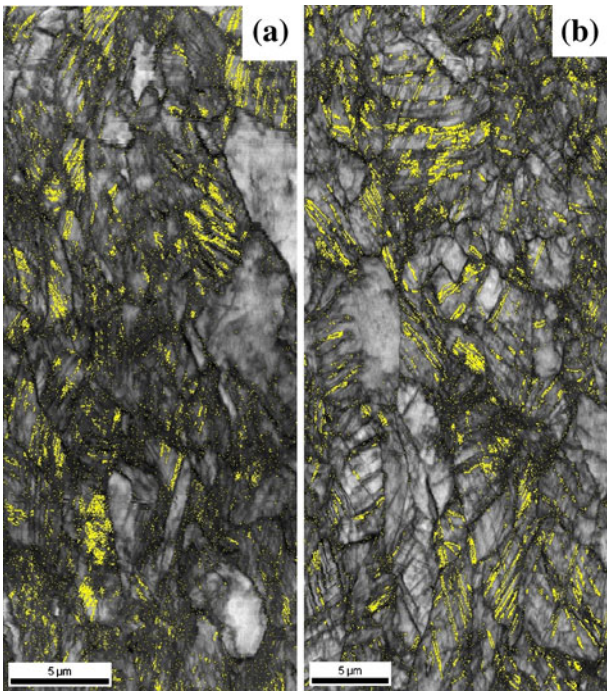


Fig. 16—IQ maps of HR steel E5 deformed at (a) 233 K (−40 °C) and (b) 373 K (100 °C) by an SR ($\dot{\epsilon}$) of 0.003 s^{-1} for the D1 grain-size distribution after fracture ($\epsilon > 0.35$). The detectable twin boundaries are marked in yellow. The scanned area has dimensions of (a) $15 \mu\text{m} \times 35 \mu\text{m}$ and (b) $20 \mu\text{m} \times 45 \mu\text{m}$, step size of 25 nm.

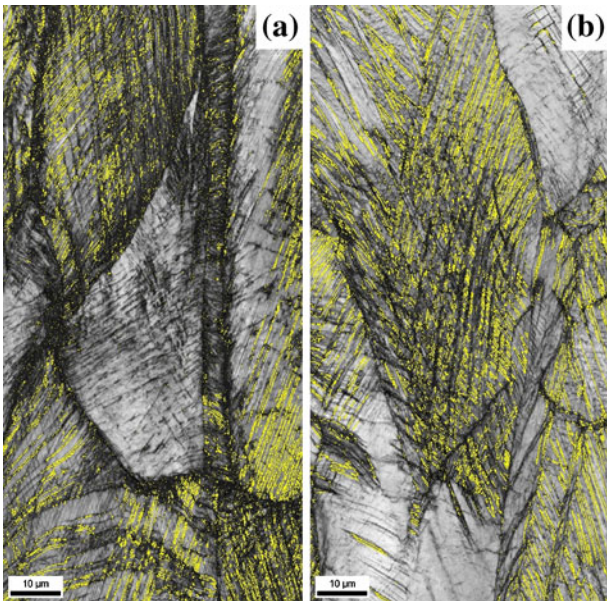


Fig. 17—IQ maps of HR steel E5 deformed at (a) 233 K (−40 °C) and (b) 373 K (100 °C) by an SR ($\dot{\epsilon}$) of 0.003 s^{-1} for the D3 grain-size distribution after fracture ($\epsilon > 0.45$). The detectable twin boundaries are marked in yellow. The scanned area has dimensions of (a) $65 \mu\text{m} \times 120 \mu\text{m}$ and (b) $75 \mu\text{m} \times 150 \mu\text{m}$, step size of 100 nm.

factor for defining the twinning stress is the higher SRO in E1. This analysis, however, must be validated by further investigation.

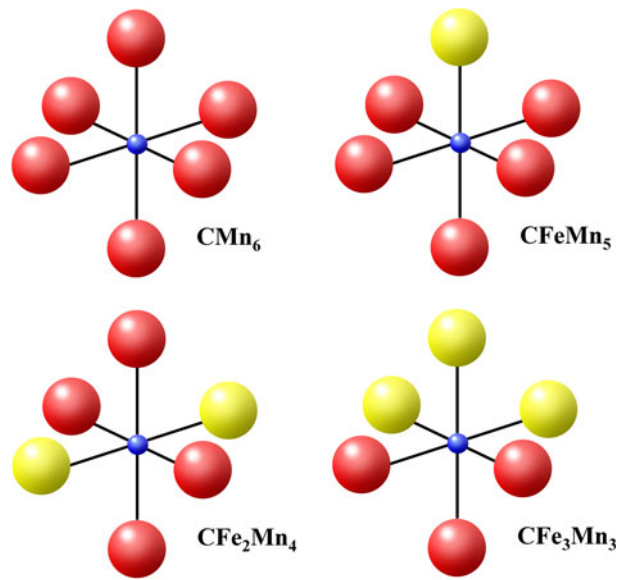


Fig. 18—Most stable atomic configurations in the $\text{CFe}_{6-x}\text{Mn}_x$ octahedral clusters, reconstructed based on the work of von Appen and Dronskowski.^[55] Iron, manganese, and carbon atoms are shown by yellow, red, and blue spheres, respectively.

The work hardening in high-manganese TWIP steels is initially driven by planar dislocation glide before the onset of deformation twinning due to the interaction of SRO and dislocations.^[49] The process is not dependent on other parameters, such as SFE or the value of the yield stress as discussed by Gerold and Karnthaler,^[28] even though they may support the arrangement of dislocations in planar arrays. Therefore, the work-hardening rate for E1 steel is consistently higher than that of E2 steel, even from the onset of plastic deformation (Figure 5).

B. Work-hardening Behavior of Iso-TOI TWIP Steels (E3/E4 and L1/L2)

The substantial decrease in the SFE value is likely to be the principal reason for the higher work-hardening rate and earlier onset of stage C^[60] in the work-hardening rate diagrams of E3 steel compared with E4 steel in Figure 7 (iso-TOI steels). The EBSD IQ maps of Figures 8 and 9 show a similar evolution/intensity of deformation twinning for logarithmic strains of 0.02, 0.10, and 0.20. In the case of the lower SFE scenario (E3), the deformation twins are finely structured, while in the higher SFE scenario (E4), the deformation twins are longer and widely separated. To explain this difference, Christian^[75] suggested that with the increasing SFE, the nucleation stress for twinning increases rapidly compared with the propagation stress. It was observed that in the very low-SFE regime, almost homogenous deformation, the consequence of fine-scale localized twinning throughout the specimen, occurs. This conclusion is consistent with the comparison of the observations in Figure 8(c) (SFE of 21 mJ/m^2) with those in Figure 9(c) (SFE of 35 mJ/m^2). In addition, by comparing the work-hardening rate diagrams of the L1

and L2 steels (Figure 10(a)), the same conclusion can be drawn: at a constant TOI value, the increase of SFE decreases the work-hardening rate. Other investigators^[16,36] have discussed the effect of aluminum on increasing the SFE value and decreasing the interaction time between SFs and point defect complexes,^[36] along with its effect on the internal structure of twins (which can reduce the work-hardening rate). However, increasing the aluminum content above 8 wt pct while increasing the carbon and manganese content, as seen in recently developed MBIP, can result in the formation of κ carbides, thereby enhancing the planar dislocation glide and increasing the work-hardening rate. Because the formation of κ carbides has not been reported in the composition range of high-manganese TWIP steels, it is not considered for the Fe-Mn-Al-C TWIP steels in the present work.

C. Work-hardening Behavior of TWIP Steels with Different SFE and TOI Values

The lower work-hardening rate for L4 steel than for L3, despite the lower SFE value of L4 (35 mJ/m² compared to 44 mJ/m²), can be explained by consideration of the formation of CFe_{6-x}Mn_x clusters in a group of 100 atoms for the different steels used in this study. As depicted in Figure 19, the maximum number of CMn₆ clusters, which can define the SRO in Fe-Mn-C TWIP steels, increases from 1 (for the E2 steel) to approximately 3 (for steels E1, E3, E4, E5, L1, and L3) and drops to 2 (for L4 steel) as the TOI value increases from 0.05 to 0.46. As explained earlier, the shortage of carbon atoms for TOI < 0.1 and the shortage of manganese for TOI > 0.3 decrease the maximum possible population of ordered zones with CFe_{6-x}Mn_x composition. Therefore, because L4 steel is in the TOI > 0.3 domain, while L3 steel is located in the TOI < 0.3 domain, L3 steel shows a higher work-hardening rate because it has more ordered zones, higher dislocation density for a given strain, and a more

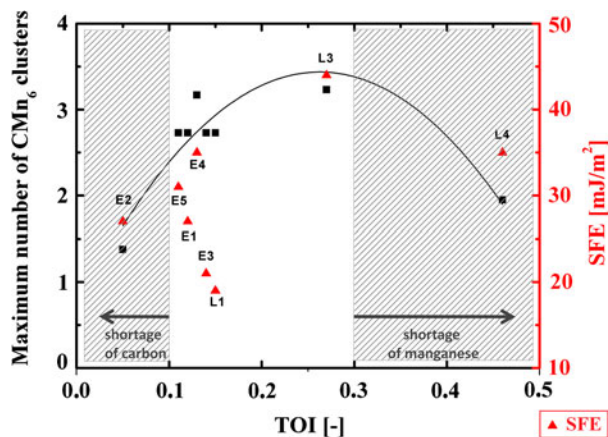


Fig. 19—Maximum number of possible CMn₆ octahedral clusters in a 100-atom sample of steels E1 to E5, L1, L3, and L4. The black squares indicate the number of clusters, while the red triangles show the relevant SFE values for the given steels. The cross-hatched areas are ranges of TOI that result in a lower number of CMn₆ clusters.

pronounced strengthening due to the interaction of dislocations and SRO. Moreover, it is seen that the variation trend in the thermodynamically calculated SFE values of different steels, based on the assumption of regularity in the solid solution, in Figure 19 show no correlation with the maximum number of CMn₆ clusters.

D. Change of Work-hardening Rate by Decreasing SFE and Increasing TOI

A simultaneous decrease of SFE (from 50 to 31 mJ/m²) and increase of TOI (from 0.07 to 0.11) in E5 steel compared to E6 steel (Figure 11(b)) resulted in an increased occurrence of deformation twinning and SRO, thereby increasing the work-hardening rate ($\epsilon > 0.20$) to 2600 MPa. In addition, the serrations on the flow curve are seen in E5 steel and not in the high-SFE aluminum-containing E6 TWIP steel because of the limited DSA mechanism in the low-TOI regime. According to Kim *et al.*,^[36] the increase of the SFE value by the addition of aluminum causes the delayed onset of serrated flow, which may be another cause for the observation of smooth flow in E6 steel.

E. Work-hardening Behavior Across the Range of Deformation Temperatures, Applied Strain Rates, and Grain-Size Regimes

The drop observed in the work-hardening rate diagrams (Figures 13(a) and (b)) with increasing temperature and grain size can be attributed to the limitation of deformation twinning due to a higher SFE value (in the case of increasing temperature)^[5] and the earlier saturation of deformation twinning (in the case of increasingly coarse grains).^[20] As seen in the IQ map of Figure 15, deformation twinning in the coarse-grained regime exhibits a sudden increase in the activation of non-coplanar twinning systems and final saturation (as seen in the temperature range between 233 K (-40 °C) and 373 K (100 °C) in the IQ maps of Figure 17). This behavior can also be indicated by the earlier reduction of the work-hardening rate. The finest grain-size regime (D1) in Figure 13(b) shows a high work-hardening rate, which, according to Reference 76, is achieved by a limited dynamic recovery due to the low SFE, despite the limited deformation twinning (IQ maps of Figure 16).

The gradual decrease of the work-hardening rate for the applied strain rate of 0.01 s⁻¹ compared to lower strain-rate scenarios is due to the sequential and localized high-temperature motion of deformation bands and the resultant gradual increase of the SFE value, which is more pronounced at higher applied strain rates (Part II provides detailed information).

As a complementary comment, it is worth noting that the intermediate grain-size regime shows the highest fracture strain, presumably due to its longer lasting deformation twinning. For the same reason, the fracture strain of the sample deformed at 373 K (100 °C) with the highest SFE value was the highest of all testing temperatures (Figure 13(a)). This result is consistent with the explanation of Huang *et al.*,^[77] which suggests

that the reduction of twinning may have a positive impact by increasing fracture elongation.

F. A Commentary Concerning Austenite Grain Size and SFE Value

By consideration of the microstructural evolution and twinning activity in the finest grain-size regime of steel E5 (D1 with the average value of about $2\ \mu\text{m}$) in Figure 16, as also suggested by other investigators,^[78] together with the increase in the work-hardening rate level by grain refinement in Figure 13(b), the previously proposed role of grain size on the SFE value (increase of SFE by grain refinement)^[5,21,79] is doubted. By comparing Figures 13(a) and (b), it is seen that the decrease of SFE by decreasing temperature has almost the same influence as grain refinement on increasing the work-hardening rate level. It is concluded that the SFE value is mainly changed by variations in chemical composition and temperature. The grain-size effect, on the other hand, is mostly observed with respect to the changes in the activation or saturation of deformation twinning in TWIP steels (Figures 14 and 15). In addition, the effect of grain size on the twinning stress according to the Hall–Petch relationship was reported.^[78]

G. Work-hardening Rate Diagrams of TWIP Steels: Stages and Mechanisms

The discussed effects of SFE, deformation temperature, austenite grain size, applied strain rate, and TOI on the work-hardening rate diagrams of TWIP steels are summarized in the schematic diagram shown in Figure 20. The deformation twinning in TWIP steels reportedly happens in the early moments of plastic deformation,^[60,61] which has been marked as stage A. As explained earlier (Figure 13(b)), in the case of coarse-grained regimes, the activation of non-coplanar twin systems can happen in the onset of stage B. This observation is in contrast with the steps suggested by Asgari *et al.*,^[80] in which stages C and D are described as the times where twin intersection and twinning rate decrease are most likely to occur. The onset of stage B was shifted to lower values of strain by increasing the grain size, which can be related to the sudden burst of deformation twinning in the coarse-grained regime. The decrease of SFE, deformation temperature, applied strain rate, and grain size, together with the increase of TOI (for $\text{TOI} < 0.3$), results in an increased work-hardening rate level in stage B. Finally, the increase of temperature, which increases the SFE as well, and an intermediate grain size (of approximately 20 to $30\ \mu\text{m}$) improve the fracture strain. However, it must be pointed out that the increase of SFE is not a universal predictor of better plasticity, as the addition of aluminum to L2 steel slightly compromised the plasticity, despite increasing the SFE value.

A very recent elaborate work by Gutierrez-Urrutia and Raabe^[81] on Fe-22 wt pct Mn-0.6 wt pct C TWIP steel illustrated five main domains for the work-hardening rate diagrams (Figure 21): (a) initial downhill, which is mostly controlled by the dynamic recovery;

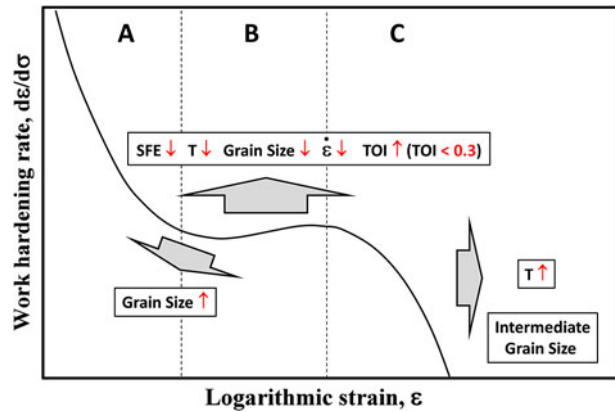


Fig. 20—Schematic representation of variations in the work-hardening rate diagrams caused by changing the SFE value, the deformation temperature (T), the austenite grain size, the applied strain rate ($\dot{\epsilon}$), and the TOI value.

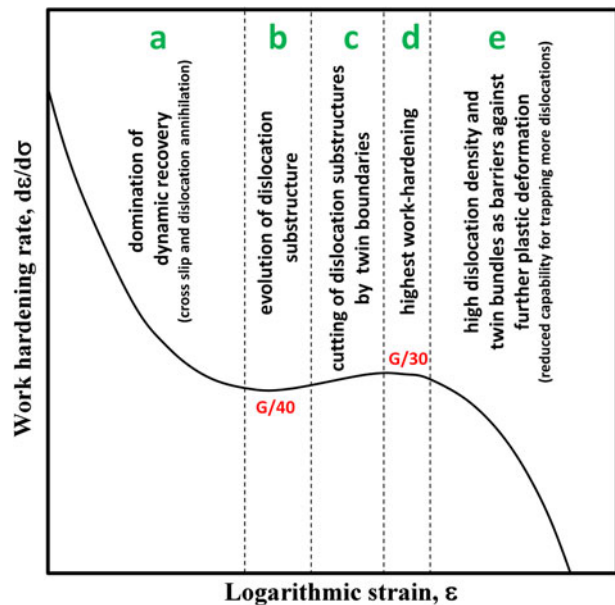


Fig. 21—Different stages of work hardening and the relevant microstructural phenomena in Fe-22 wt pct Mn-0.6 wt pct C TWIP steel, as described by Gutierrez-Urrutia and Raabe.^[81] G in the diagram stands for the shear modulus.

evolution of the dislocation substructures (work-hardening rate of about $G/40$); (c) cutting of dislocation substructures by twin boundaries, which continues up to stage (d); (d) definition of the maximum work-hardening rate ($G/30$, which is close to the values reported for Hadfield steels); and (e) final downhill of the work-hardening rate due to an increased dislocation density and the presence of twin bundles as barriers against the continuation of plastic deformation.^[81] The shape of the work-hardening rate diagrams of TWIP steels E1 and E2 (Figure 5), L3 and L4 (Figure 10(b)), and E5 and E6 (Figures 11(b) and 13) clearly include the proposed stages of the work hardening by Gutierrez-Urrutia and Raabe,^[81] which might be considered as a hint to assume

their given reasoning to be plausible in a broad range of TWIP steel compositions. However, further research is required to validate experimentally the consistency of the mentioned microstructural features during the plastic deformation of different TWIP steels.

VI. CONCLUSIONS

Based on the given methodology in the present work and by consideration of a group of ten high-manganese TWIP steels, the work-hardening behavior of this group of materials was investigated. The following results was demonstrated.

1. A unified approach in terms of deformation twinning (controlled by SFE) together with DSA and planar dislocation glide (controlled by SRO of manganese and carbon atoms) was required to explain the variations in the work-hardening rate diagrams of TWIP steels across an extensive range of chemical compositions within the Fe-Mn-C and Fe-Mn-Al-C systems.
2. The previously proposed mechanism maps were updated using the parameters extracted from the SGTE dataset, and by including the dimensionless TOI parameter to account for the variations in the work-hardening rate diagrams of iso-SFE TWIP steels. Second, it was shown that the shortage of carbon in the TOI range below 0.1 and the shortage of manganese in the TOI range above 0.3 could decrease the strengthening that was otherwise achieved by the interaction of dislocations with SRO.
3. The increase of temperature or grain size was shown to reduce the work-hardening because of either the limitation of deformation twinning (because of increase in the SFE value) or the sudden burst and saturation of deformation twinning (in the coarse-grained regime).
4. The low SFE value, in general, increased the work-hardening rate and caused the earlier onset of stage C. The increase of SFE (by increasing the temperature or the manganese and carbon content) improved the fracture strain, despite the decrease of the work-hardening rate, which was in contrast with the published results concerning the effect of aluminum (which increases the SFE as well) in TWIP steels. This contradiction could be related to the role of aluminum in limitation of the DSA mechanism and not necessarily its effect on the SFE value, which requires further investigation.

ACKNOWLEDGMENT

The authors gratefully acknowledge the financial support of the Deutsche Forschungsgemeinschaft (DFG) within the Collaborative Research Center (SFB) 761 “Steel-ab initio.”

REFERENCES

1. G. Frommeyer and U. Brück: *Steel Res. Int.*, 2006, vol. 77, pp. 627–33.
2. O. Grässel, L. Krüger, G. Frommeyer, and L.W. Meyer: *Int. J. Plast.*, 2000, vol. 16, pp. 1391–1409.
3. S. Allain, J.-P. Chateau, and O. Bouaziz: *Mater. Sci. Eng. A*, 2004, vols. 387–389, pp. 143–47.
4. O. Bouaziz, S. Allain, and C. Scott: *Scripta Mater.*, 2008, vol. 58, pp. 484–87.
5. A. Saeed-Akbari, J. Imlau, U. Prahl, and W. Bleck: *Metall. Mater. Trans. A*, 2009, vol. 40A, pp. 3076–90.
6. J. Nakano and P.J. Jacques: *CALPHAD*, 2010, vol. 34, pp. 167–75.
7. S. Curtze, V.T. Kuokkala, A. Oikari, J. Talonen, and H. Hänninen: *Acta Mater.*, 2011, vol. 59, pp. 1068–76.
8. O. Bouaziz, C.P. Scott, and G. Petitgand: *Scripta Mater.*, 2009, vol. 60, pp. 714–16.
9. J.W. Christian and S. Mahajan: *Prog. Mater. Sci.*, 1995, vol. 39, pp. 1–157.
10. H. Idrissi, L. Ryelandt, M. Veron, D. Schryversa, and P.J. Jacques: *Scripta Mater.*, 2009, vol. 60, pp. 941–44.
11. L. Remy: *Scripta Metall. Mater.*, 1977, vol. 11 (3), pp. 169–72.
12. L. Remy: *Acta Metall.*, 1978, vol. 26, pp. 443–51.
13. L. Remy and A. Pineau: *Mater. Sci. Eng. A*, 1977, vol. 28, pp. 99–107.
14. S. Mahajan and G.Y. Chin: *Acta Metall.*, 1973, vol. 21, pp. 1353–63.
15. S. Kibey, J.B. Liu, D.D. Johnson, and H. Sehitoglu: *Acta Mater.*, 2007, vol. 55, pp. 6843–51.
16. H. Idrissi, K. Renard, D. Schryvers, and P.J. Jacques: *Scripta Mater.*, 2010, vol. 63, pp. 961–64.
17. H. Idrissi, K. Renard, L. Ryelandt, D. Schryvers, and P.J. Jacques: *Acta Mater.*, 2010, vol. 58, pp. 2464–76.
18. G. Frommeyer, U. Brück, and P. Neumann: *ISIJ Int.*, 2003, vol. 43 (3), pp. 438–46.
19. H. Ding, Z. Tang, W. Li, M. Wang, and D. Song: *J. Iron Steel Res. Int.*, 2006, vol. 13 (6), pp. 66–70.
20. A. Saeed-Akbari: *Mechanism Maps, Mechanical Properties, and Flow Behavior in High-Manganese TRIP/TWIP and TWIP Steels*, Shaker Verlag, Aachen, 2011.
21. Y.K. Lee and C.S. Choi: *Metall. Mater. Trans. A*, 2000, vol. 31A, pp. 355–60.
22. G. Dini, A. Najafzadeh, R. Ueji, and S.M. Monir-Vaghefi: *Mater. Sci. Eng. A*, 2010, vol. 527, pp. 2759–63.
23. T.S. Byun: *Acta Mater.*, 2003, vol. 51, pp. 3063–71.
24. O. Bouaziz and N. Guelton: *Mater. Sci. Eng. A*, 2001, vols. 319–321, pp. 246–49.
25. L. Chen, Han-soo Kim, Sung-Kyu Kim, and B.C. De-Cooman: *ISIJ Int.*, 2007, vol. 47, pp. 1804–12.
26. P.H. Adler, G.B. Olsen, and W.S. Owen: *Metall. Trans. A*, 1986, vol. 17A, pp. 1725–37.
27. L.G. Stepankiy: *Scripta Mater.*, 2009, vol. 61, pp. 947–50.
28. V. Gerold and H.P. Karnthaler: *Acta Metall.*, 1989, vol. 37, pp. 2177–83.
29. J.D. Yoo and K. Park: *Mater. Sci. Eng. A*, 2008, vol. 496, pp. 417–24.
30. J.D. Yoo, S.W. Hwang, and K. Park: *Mater. Sci. Eng. A*, 2009, vol. 508, pp. 234–40.
31. K. Choi, C. Seo, H. Lee, S.K. Kim, J.H. Kwak, K.G. Chin, K. Park, and N.J. Kim: *Scripta Mater.*, 2010, vol. 63, pp. 1028–31.
32. Y.N. Dastur and W.C. Leslie: *Metall. Trans. A*, 1981, vol. 12A, pp. 749–59.
33. B.K. Zuidema, D.K. Subramanyam, and W.C. Leslie: *Metall. Mater. Trans. A*, 1987, vol. 18A, pp. 1629–39.
34. T. Shun, C.M. Wan, and J.G. Byrne: *Acta Metall. Mater.*, 1992, vol. 50 (12), pp. 3407–12.
35. J. Kim, L. Chen, H. Kim, S.K. Kim, Y. Estrin, and B.C. De-Cooman: *Metall. Mater. Trans. A*, 2009, vol. 40A, pp. 3147–58.
36. J. Kim, S.J. Lee, and B.C. De-Cooman: *Scripta Mater.*, 2011, vol. 65, pp. 363–66.
37. K. Renard, S. Ryelandt, and P.J. Jacques: *Mater. Sci. Eng. A*, 2010, vol. 527, pp. 2969–77.
38. E. Bayraktar, C. Levailant, and S. Altintas: *J. Phys. IV*, 1993, vol. 3, pp. 61–66.

39. *Annual Book of ASTM Standards*, ASTM INTERNATIONAL, Philadelphia, PA, 2004, vol. 3, No. 01, E112-96, p. 227.
40. A.T. Dinsdale: *CALPHAD*, 1991, vol. 15 (4), pp. 317-425.
41. S. Allain, J.-P. Chateau, O. Bouaziz, S. Migot, and N. Guelton: *Mater. Sci. Eng. A*, 2004, vol. 387389, pp. 158-62.
42. A.S. Hamada: Doctoral Thesis, University of Oulu, Oulu, Finland, 2007.
43. S. Vercammen: Doctoral Thesis, Katholieke Universiteit Leuven, Leuven, Belgium, 2004.
44. O. Bouaziz, S. Allain, C.P. Scott, P. Cugy, and D. Barbier: *Curr. Opin. Solid St. M.*, 2011, vol. 15 (4), pp. 141-68.
45. I. Karaman, H. Sehitoglu, Y.I. Chumlyakov, and H.J. Maier: *JOM*, 2002, July, pp. 31-37.
46. H. Suzuki: *J. Phys. Soc. Jpn.*, 1962, vol. 17 (2), pp. 322-25.
47. I. Karaman, H. Sehitoglu, Y.I. Chumlyakov, H.J. Maier, and I.V. Kireeva: *Scripta Mater.*, 2001, vol. 44, pp. 337-43.
48. Y.N. Petrov: *Scripta Mater.*, 2005, vol. 53, pp. 1201-06.
49. K.T. Park, K.G. Jin, S.H. Han, S.W. Hwang, K. Choi, and C.S. Lee: *Mater. Sci. Eng. A*, 2010, vol. 527, pp. 3651-61.
50. W.S. Owen and M. Grujicic: *Acta Mater.*, 1999, vol. 47 (1), pp. 111-26.
51. J. Kim, Y. Estrin, H. Beladi, S. Kim, K. Chin, and B.C. De Cooman: *Mater. Sci. Forum*, 2010, vol. 654656, pp. 270-73.
52. Y. Estrin and L.P. Kubin: *Acta Metall.*, 1986, vol. 34, pp. 2455-64.
53. L.P. Kubin and Y. Estrin: *Acta Metall.*, 1990, vol. 38, pp. 697-708.
54. O. Bouaziz, H. Zurob, B. Chehab, J.D. Embury, S. Allain, and M. Huang: *Mater. Sci. Technol.*, 2011, vol. 27 (3), pp. 707-09.
55. J. von Appen and R. Dronskowski: *Steel Res. Int.*, 2011, vol. 82 (2), pp. 101-07.
56. E.P. Kwon, S. Fujieda, K. Shinoda, and S. Suzuki: *Mater. Sci. Eng. A*, 2011, vol. 528, pp. 5007-17.
57. R. Petrov, L. Kestens, A. Wasilkowska, and Y. Houbaert: *Mater. Sci. Eng. A*, 2007, vol. 447, pp. 285-97.
58. A. Weidner, S. Martin, V. Klemm, U. Martin, and H. Biermann: *Scripta Mater.*, 2011, vol. 64, pp. 513-16.
59. D.R. Steinmetz and S. Zaeferrer: *Mater. Sci. Technol.*, 2010, vol. 26 (6), pp. 640-45.
60. D. Barbier, N. Gey, S. Allain, N. Bozzolo, and M. Humber: *Mater. Sci. Eng. A*, 2009, vol. 500, pp. 196-206.
61. A.S. Hamada, L.P. Karjalainen, A. Ferraiuolo, J.G. Sevillano, F.D.L. Cuevas, G. Pratalongo, and M. Reis: *Metall. Mater. Trans. A*, 2010, vol. 41A, pp. 1102-08.
62. M.R. Barnett: *Scripta Mater.*, 2008, vol. 59, pp. 696-98.
63. Y.N. Petrov: *Z. Metallkd.*, 2003, vol. 94 (9), pp. 1012-16.
64. A. Dumay, J.-P. Chateau, S. Allain, S. Migot, and O. Bouaziz: *Metall. Mater. Trans. A*, 2008, vols. 483-484, pp. 184-87.
65. L. Remy, A. Pineau, and B. Thomas: *Mater. Sci. Eng.*, 1978, vol. 36, pp. 47-63.
66. G.W. Han, I.P. Jones, and R.E. Smallman: *Acta Mater.*, 2003, vol. 51, pp. 2731-42.
67. A. Herschitz and D.N. Seidman: *Acta Metall.*, 1985, vol. 33 (8), pp. 1547-63.
68. J.C. Fisher: *Acta Metall.*, 1954, vol. 2 (3), pp. 368-69.
69. P.A. Flinn: *Acta Metall.*, 1958, vol. 6 (10), pp. 631-35.
70. S. Asgari, E. El-Danaf, E. Shaji, S.R. Kalidindi, and R.D. Doherty: *Acta Mater.*, 1998, vol. 46 (16), pp. 5795-5806.
71. Y. Tomokiyo, N. Kuwano, and T. Eguchi: *Trans. JIM*, 1975, vol. 16, pp. 489-99.
72. G. Thomas: *Acta Metall.*, 1963, vol. 11, pp. 1369-71.
73. J.M. Poplewell and J. Crane: *Metall. Trans.*, 1971, vol. 2, pp. 3411-20.
74. I. Karaman, H. Sehitoglu, H.J. Maier, and Y.I. Chumlyakov: *Acta Mater.*, 2001, vol. 49, pp. 3919-33.
75. J.W. Christian: *The Theory of Transformations in Metals and Alloys*, 1st ed., Pergamon Press Ltd., Oxford, United Kingdom, 1965, pp. 743-77.
76. R. Ueji, N. Tsushida, D. Terada, N. Tsuji, Y. Tanaka, A. Takemura, and K. Kunishige: *Scripta Mater.*, 2008, vol. 59, pp. 963-66.
77. B.X. Huang, X.D. Wang, and Y.H. Rong: *Metall. Mater. Trans. A*, 2008, vol. 39A, pp. 717-24.
78. I. Gutierrez-Urrutia, S. Zaeferrer, and D. Raabe: *Mater. Sci. Eng. A*, 2010, vol. 527, pp. 3552-60.
79. P.Y. Volosevich, V.N. Grindnev, and Y.N. Petrov: *Phys. Met. Metallogr.*, 1976, vol. 42, pp. 126-30.
80. S. Asgari, E. El-Danaf, S.R. Kalidindi, and R. Doherty: *Metall. Mater. Trans. A*, 1997, vol. 28A, pp. 1781-94.
81. I. Gutierrez-Urrutia and D. Raabe: *Acta Mater.*, 2011, vol. 59, pp. 6449-62.